Size and Composition Dependence of Oxygen Reduction Reaction Catalytic Activities of Mo-doped PtNi/C Octahedral Nanocrystals

Shlomi Polani,[*a] Katherine E. MacArthur,[b] Malte Klingenhof,[a] Xingli Wang,[a] Paul Paciok,[b] Lujin Pan,[a] Quanchen Feng,[a] Attila Kormányos,[c] Serhiy Cherevko,[c] Marc Heggen,[*b] and Peter Strasser[*a]

[a]Electrochemical Energy, Catalysis and Material Science Laboratory, Department of Chemistry, Technical University Berlin, 10623 Berlin, Germany

[b]Ernst-Ruska Centre for Microscopy and Spectroscopy with Electrons and Peter Grünberg Institute, Forschungszentrum Jülich GmbH, 52425 Jülich, Germany

[c]*Helmholtz-Institute Erlangen-Nürnberg for Renewable Energy (IEK-11), Forschungszentrum Jülich, 91058 Erlangen, Germany*

KEYWORDS: PtNiMo octahedra, synthesis, oxygen reduction, metal dissolution, stability

A variety of synthesis protocols for octahedral PtNi nanocatalysts have led to remarkable improvements in platinum mass and specific activities for the oxygen reduction reaction. Nevertheless, the values achieved are still only one tenth of the activity measured from Pt_3Ni single-crystal (111) surfaces. These particles lose activity during potential cycling, primarily due to Ni leaching and subsequent loss of shape. Here, we present the syntheses and high catalytic oxygen reduction reaction activities of molybdenum-doped PtNi octahedral catalysts with different sizes (6-14 nm) and compositions. We show that the Mo-doped, Ni-rich, PtNi octahedral catalysts exhibit enhanced stability over their un-doped counterpart. Scanning transmission electron microscopy with energy dispersive X-ray analysis reveals the particular elemental distribution for the size and composition of the different catalysts. By combining high resolution compositional analysis with electrochemical measurements and on-line inductively coupled plasma mass spectrometry, it was possible to correlate the size, morphology and composition with the oxygen reduction reaction activities before and after accelerated stress tests. The octahedral catalysts show high electrochemical surface areas and increasing specific activity with increasing surface area of the (111) facets and Ni content, leading to high mass activities. These results demonstrate the advantages of increasing the (111) surface area and Ni content of PtNi nano-octahedral catalysts to improve the performance and stability for oxygen reduction reaction.

Proton exchange membrane fuel cells (PEMFCs), considered a clean power source for stationary and mobile devices, have been a focal point for researchers in the last decades. The primary technical challenges for automotive applications are durability and cost. The latter relates to the sluggish oxygen reduction reaction (ORR) rate at the cathode, which necessitates the deployment of high Pt mass loadings. The ORR is a structure-sensitive process, that is, its rate depends on the crystallographic orientation of the Pt surface. The ORR activity increases in the order of (100) < (110) = (111).[1] Studies conducted on Pt-based bimetallic catalysts showed volcano-type catalytic ORR rates, where the alloying of Pt with certain 3d-transition metals or lanthanides boosted the ORR activity.[2-5] Structurally, the formation of a surface lattice-strained monoatomic Pt-skin upon thermal annealing, or else the formation of a surface lattice-strained Pt-shell structure upon selective 3d metal leaching were both held responsible for the high experimental ORR reactivity. This was because these strained surfaces featured downshifted d-band centers relative to pure Pt, weakening chemisorption of reactive intermediates. In the wake of this insight, the "materials-by-design"[6] strategy, which focuses on the transfer of single-crystal knowledge to nanoscale materials, led to heightened interest in small, 4-9 nm edge length, Pt-rich, shape-controlled, octahedral (oh-) PtNi nanoparticles (NPs) enclosed with facets. While these nano-catalysts showed increases in their specific ORR activities over Pt and spherical PtNi NPs, [7, 8] they suffered from structural instability and compositional inhomogeneity, which is why they fell short of the intrinsic ORR activity of the experimental ORR activity of Pt_3Ni (111) single crystal.[7]

There is consensus that larger and compositionally uniform PtNi octahedral catalysts are needed to overcome the cost and degradation issues.[9-15] The most widely applied synthetic protocols for oh-PtNi NPs involve the reduction of $Pt(acac)_2$ and $Ni(acac)_2$ using Dimethylformamide (DMF) as the solvent and reducing agent. The synthesis has been typically carried out in a sealed vessel (autoclaves, pressure flasks or vials) and the reaction temperature has been generally above the boiling points of both the DMF (153 °C) and the acetylacetonate ligand (140 °C).[16-19] The low Ni-content of the resulting NP catalysts (to a large degree Pt_3Ni octahedra), combined with the weak reductive power of DMF raised doubts about the rate of reduction of $Ni(acac)_2$ from Ni^{II} to Ni^0 under these conditions.[18, 20] Alternatively, Pt-rich oh-PtNi NPs have been synthesized at temperatures above 200 °C using oleylamine and oleic acid as solvents and capping agents, and with or without tungsten hexacarbonyl as reducing and shape-directing agent.[21-25] Wu et al.[26] proposed the use of benzyl alcohol (BA) as both solvent and reducing agent to produce larger bimetallic oh-PtNi NP catalysts (11.8 ± 1.2 nm apex to opposite apex). However, these oh-PtNi NP catalysts were never studied for their oxygen electroreduction performance.[27] The structural degradation of compositionally inhomogeneous DMF-derived bimetallic oh-PtNi NPs series was tracked by monitoring their catalytic activities in conjunction with their compositional and structural evolutions.[16] The Ni-rich facet centers showed preferred leaching, resulting in a concave curvature or hexapod skeleton in which the catalytically active (111) facets were lost, resulting in decreased ORR activity.

Doping strategies for oh-PtNi NPs with a third metal like Mo, Rh or Ga, were proposed to improve ORR reactivity, facet stability and long-term durability.[28] Mo doping of oh-Pt_3Ni catalysts[29] (two-step synthesis, 48 h) was reported with high, yet never re-produced, ORR specific (SA) and mass (MA) activities (10.3 mA cm_{Pt}^{-2} and 6.98 A mg_{Pt}^{-1} @0.9 V_{RHE}, respectively). Cao and Mueller,[30] presented computations, that suggested that surface Mo oxides on the Mo-doped oh-PtN/C NPs caused stabilization, while sub-surface Ni stabilized under-coordinated Pt sites. Subsequently, Jia et al.[31] demonstrated that the oh-Pt_3Ni (111)-like near-surface structure and hence the octahedral shape is stabilized by the doping thanks to a retention of sub-surface Ni atoms in acidic media. Dionigi et al.[32] later demonstrated and confirmed the high durability of Mo-doped PtNi/C octahedral catalyst. The Mo-doped Pt_3Ni/C octahedral catalyst (5.8 ± 1.5 nm) showed high ORR activity (3.43 ± 0.35 A mg_{Pt}^{-1} @0.9 V_{RHE}) on the RDE level, and they were further implemented in MEA-based single fuel cell tests where they demonstrated sustained Pt MA of 0.45 A mg_{Pt}^{-1} at 0.9 V_{cell}.

Beermann et al.[33] explored surface Rh-doped PtNi octahedral catalysts with well-defined shape and composition. The Rh-doped PtNi electrocatalyst showed a unique improved activity and stability compared to the un-doped PtNi octahedral catalyst. After 30k cycles between 0.05–1.0 V_{RHE}, the activity was substantially enhanced, and the octahedral shape was almost unaffected. The enhanced durability was attributed to the suppression of surface Pt migration rather than Ni dissolution.

The SA strongly depends on the fraction of exposed (111) surface and is about an order of magnitude lower for PtNi nano-octahedral catalysts than that of bulk single-crystal Pt_3Ni (111) surfaces.[9] High turnover frequencies (~2800 s^{-1}) were reported for Pt_3Ni(111) surfaces, which, if translated to the NPs scale, correlates to 30 nm diameter octahedral catalysts.[13, 14] Moreover, the durability of Pt-based catalysts is strongly enhanced in relatively large particles such as nanostructured Pt films and large PtM NPs due to the low Pt dissolution during voltage cycling,[10-12] suggesting, that large (>30 nm edge length) octahedral particles with higher surface coordination could improve activity and durability. Generally, large (>10 nm, edge length), Ni-rich PtNi octahedral catalysts are not considered as favorable catalysts for the ORR., possibly due to synthesis' conditions constraint, or because of the low stability expected due to Ni leaching during potential cycling, from relatively small, un-doped and Ni-rich catalysts, or their combination.

Here, we investigate the relationships between synthesis, particle size, composition and catalytic ORR reactivity of ternary oh-Mo-doped PtNi/C electrocatalysts. Unlike previous studies, we focus on new synthetic control strategies to achieve NPs with larger edge lengths (≤ 14 nm) and with higher Ni-content and demonstrate their favorable size-activity relationships. We uncover on a robust, yet tunable one-pot synthesis to produce oh-PtNi(Mo)/C nanocrystals with well-defined shape and exposed facets. We show how size and composition are interlinked and

affect the ORR activity, and discuss the (111) facets size-dependent Ni segregation and dissolution during accelerated stress tests (ASTs) of the different oh-PtNi(Mo)/C nanocrystals.

Results and discussion

Synthesis and Morphology. We prepared Ni-rich binary oh-PtNi NPs (Figure S1) and ternary oh- Mo-doped PtNi nanocrystals (henceforth referred to as PtNi-6 and PtNi(Mo), respectively) using BA as both the solvent and the reducing agent, and subsequently impregnated them on a high surface area carbon support (see SI).[26, 34, 35] What sets the present synthesis pathway apart from previously documented one is the one-step, one-pot nature of the Mo-doped octahedra syntheses. As a result of this, the resulting elemental distribution of Mo is through the bulk of the nano-octahedra, in contrast to surface-doping, which was reported for the two-step synthesis for Mo-doped octahedra.[29, 36]The final carbon supported catalysts are referred to as PtNi(Mo)/C. The PtNi(Mo) active phase of the catalysts is henceforth labelled as PtNi(Mo)-L, where L signifies the mean particle edge length in nm. Low resolution transmission electron microscopy (TEM) images and particle size analysis demonstrate the uniformity of the PtNi(Mo)/C octahedral series shape and their homogenous distributions on high-surface-area carbon support (Figure 1). The corresponding narrow particle size distribution (PSD) is presented in the insets. The PtNi(Mo)/C octahedral NPs exhibit different compositions and slightly different Pt wt%, which were determined using inductively-coupled plasma optical emission spectroscopy (ICP-OES) and summarized in table S1 in the SI. Two experimental parameters were found to control particle composition and size: The Ni precursor amount and its supersaturated concentration. Tuning the amount of Ni precursor was a simple way to achieve control over composition and size. The NPs with 7.3, 10.4 and 12.4 nm NPs edge length

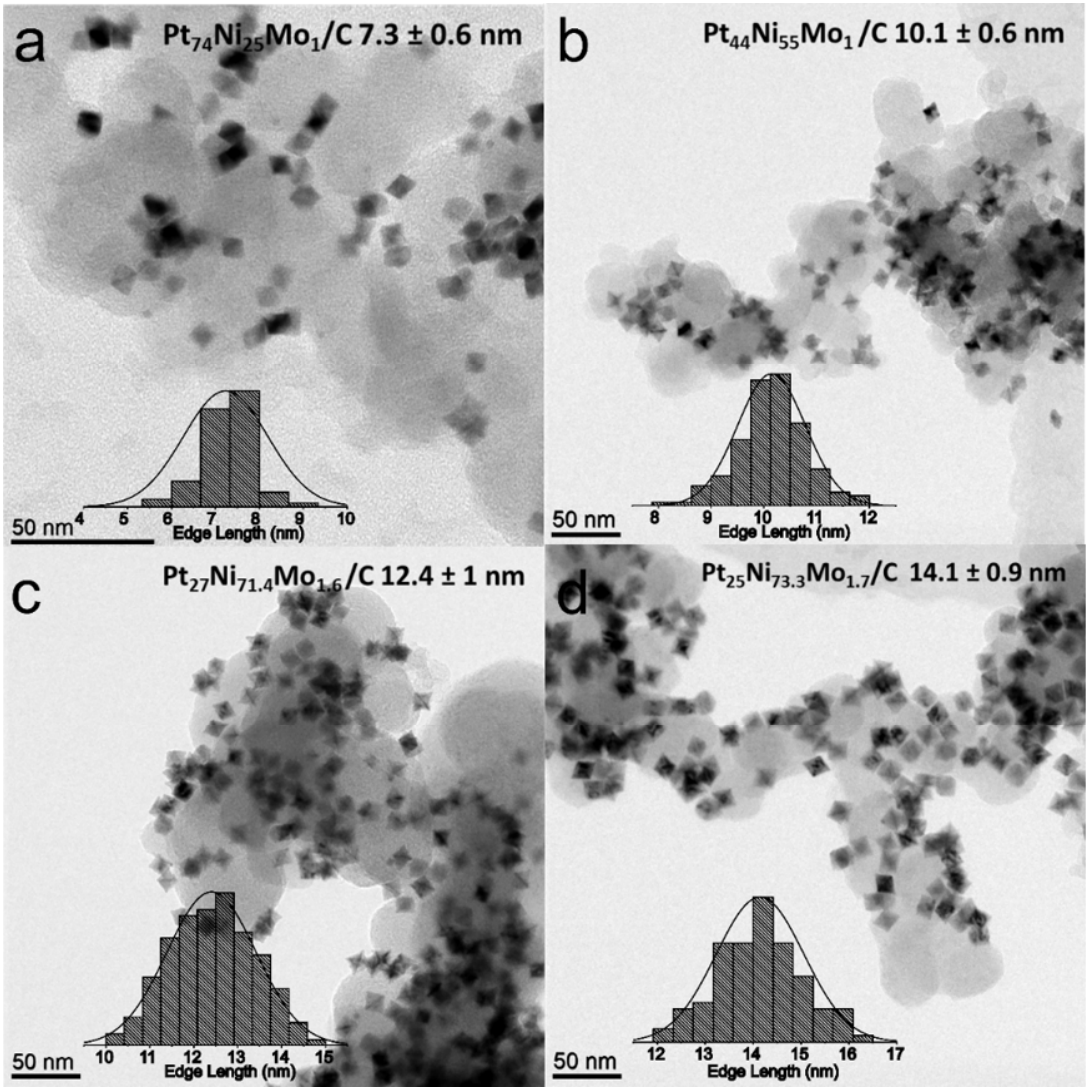

Figure 1. Transmission electron microscopy (TEM) images, atomic compositions, mean edge length and the corresponding edge length distribution histogram for PtNi(Mo)/C octahedral NPs (a) PtNi(Mo)-7 (b) PtNi(Mo)-10 (c) PtNi(Mo)-12 (d) PtNi(Mo)-14.

(referred to as PtNi(Mo)-7, -10, and -12) shown in Figure 1a–c were prepared by employing 50, 100 and 200 mg of Ni(acac)2, respectively, under otherwise constant conditions.

To rationalize the relationship between employed Ni precursor mass, resulting Ni atomic ratio, and NPs size we hypothesize that when the reaction starts, Pt and Ni possess significantly different reduction kinetics. Pt as the more noble metal initially reduces faster and nucleates to Pt-rich seeds using the reducing power of BA. The seed formation is likely enhanced by enthalpic and entropic contributions of alloying. The Ni reduction kinetics is much slower at this stage. Ni may play the role of masking Pt precursors and in doing so helps to reduce the probability of successful collisions, which moderates the reduction kinetics of Pt^{II} to Pt^{0} somewhat and, as a result of this, leads to bigger particles. This implies that the NPs growth starts after Pt nucleation, and Pt subsequently catalyzes the reduction of Ni^{II} to Ni^{0} ("noble-metal-induced reduction").[26, 37, 38] The degree of precursor saturation is also a controlling synthesis parameter for the resulting particle size. Reducing the supersaturated precursor concentration by increasing the solvent volume from 40 ml to 50 ml resulted in an increase in the size of the Ni-rich PtNi(Mo)/C NPs further from 12.4 nm to 14.1 nm (Figure 1d).[39]

The crystal phases of the obtained nanocrystalline catalysts were measured by X-ray diffraction (XRD). The XRD patterns suggest a face-centered cubic alloy structure for all nanocrystals. The patterns follow Vegard's law and are presented in Figure S2. Compared to the (111) reflection peak of pure Pt, the PtNi(Mo)-7 particles have this peak shifted to higher 2θ angles, and PtNi(Mo)-12 and PtNi(Mo)-14 are shifted even higher. The (111) peak for the PtNi-6 octahedra has the most significant shift in 2θ angles, corresponding to the highest Ni content. With the addition of Mo, no additional peak shifts could be seen in comparison to PtNi-6. PtNi(Mo)-7 peaks show higher symmetry compared to PtNi(Mo)-14, which shows a shoulder at lower 2θ angles of the (111) reflection, which may be attributed to a Pt-rich phase.

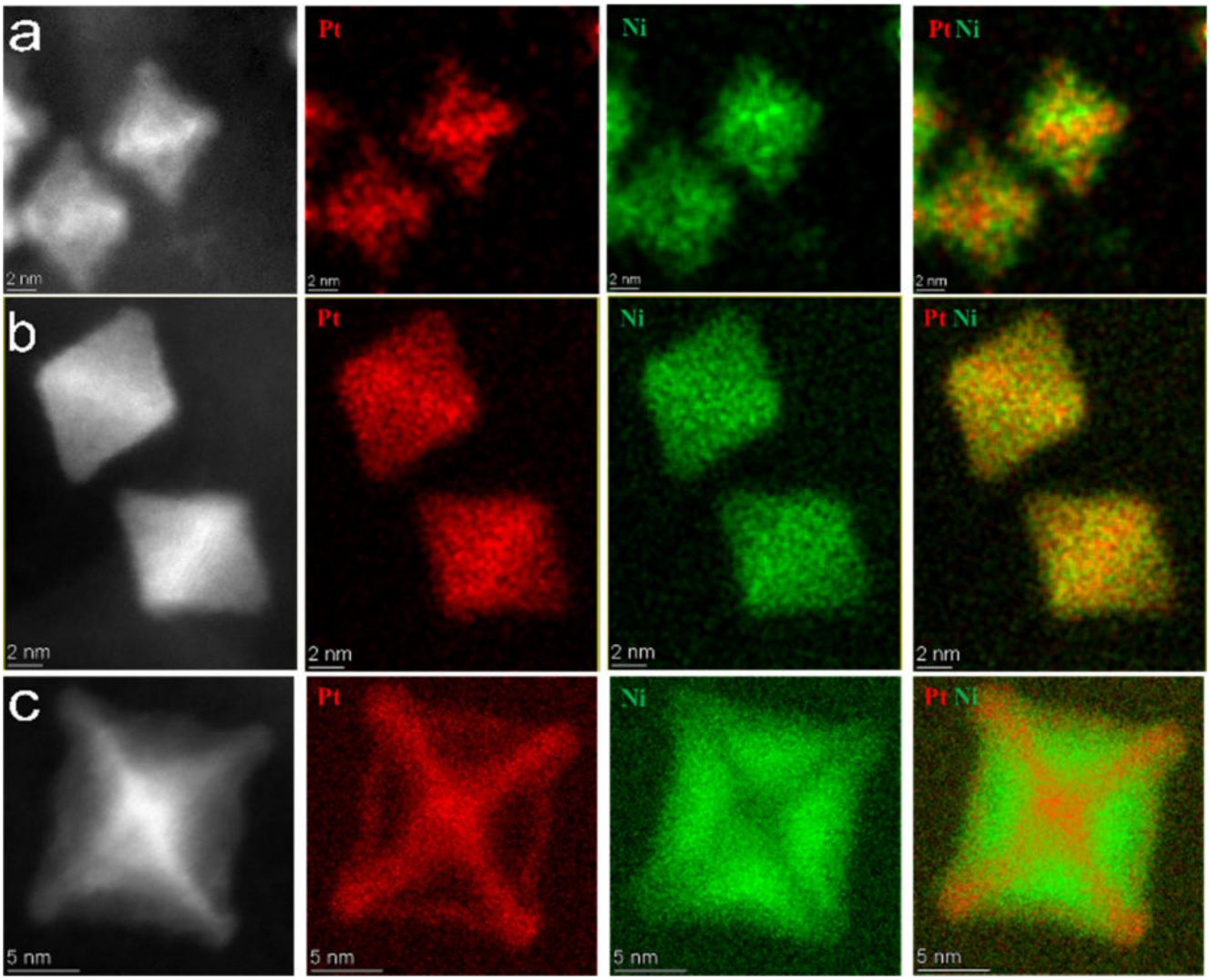

Figure 2. HAADF-STEM micrographs, STEM-EDX elemental mapping for Pt (red) and Ni (green), their overlay, for as prepared (a) PtNi-6 (b) PtNi(Mo)-7 (c) PtNi(Mo)-14.

To analyze the atomic distributions of the different catalysts, we used high angle annular dark-field (HAADF) STEM micrographs and EDX. For the oh-PtNi-6 NPs, the precise elemental segregation is not completely clear from the 2-dimensional element maps. The data suggest that Pt forms a core hexapod that sets the dimensions of the bimetallic octahedral NPs. Ni is distributed throughout the hexapod and facets of the octahedron (Figure 2 panel a). For the Mo-doped NPs, the presence of Ni-enriched facets was highly dependent on the initial Ni-loading. For PtNi(Mo)-7, STEM-EDX element mapping indicates that both Pt and Ni are evenly distributed throughout the nanocrystal framework, suggesting a uniform alloy structure and indicating comparable reduction and growth rates of Pt and Ni (Figure 2 panel b). New and unexpected compositional and morphological structures arose for the previously inaccessible, significantly larger PtNi(Mo)-12 and PtNi(Mo)-14 octahedral NPs. PtNi(Mo)-12 and PtNi(Mo)-14 (Figures S3 and 2 panel c, respectively) revealed the existence of Pt-rich edges alongside the hexapod structure, which together resembles a closed 3D Pt frame. This morphological feature was more pronounced for the PtNi(Mo)-14, presumably owing to its increased size. In contrast to PtNi(Mo)-7, their Ni atoms were invariably preferentially segregated to the {111} facets. The elemental distribution is, therefore, strongly dependent on particle size. For PtNi(Mo)-12, the ADF-STEM, EDX and line scan close to the ⟨100⟩ zone-axis in Figure S3 demonstrate the Pt frame clearly. The existence of a Pt-rich phase alongside a Ni-rich phase accounts for the asymmetry of the (111) reflection in the XRD patterns. The elemental maps of PtNi(Mo)-14 agree with the theoretically predicted and studied structure, of a so-called "Pt hexapod and edges", which was postulated using previously simulated EDX maps,[40] (see structure 4 therein).

Due to the low doping levels of Mo in the present particles, the detection and physical location of the Mo atoms is right on the limit of EDX analysis. To address this challenge, principal component analysis (PCA) was used to apply denoising to the data sets.[41] Firstly, the data was rebinned such that sufficient signal to noise per pixel was present. Then following decomposition, four components were recombined to produce a reconstructed data set. To extract counts, a model fitting was applied and the resulting elemental maps of PtNi(Mo)-14 are shown in Figure S4.[42] Here, the Mo signal was multiplied by a factor of 100 in order to be visible on the same intensity scale as the other elements, where it correlates with the Ni signal. Figure S4 shows a plot of the sum spectrum for this data set, as well as a magnified version highlighting that Mo has been detected above the level of noise, over the whole field of view.

Surface voltammetry and ORR catalysis. To establish relationships between size, composition and electrocatalytic reactivity, we tested the prepared oh-NPs catalysts using cyclic and linear scan voltammetry. Figure S5 shows the cyclic voltammetry (CV) (0.05–1 V_{RHE}) and CO-stripping voltammetry (linear scan 0.05 to 1 V_{RHE}) of the PtNi(Mo)/C series before and after electrochemical ASTs. The CVs of the catalysts displayed distinctly different characteristics. For PtNi(Mo)-7, the voltammetric H_{upd} region (0.05–0.3 V_{RHE}) was smooth and lacked the Pt(100) and Pt(110) H_{upd} peak signatures. In contrast, for PtNi(Mo)-12 and PtNi(Mo)-14 (Figure S5b and c), the (100) signature was quite visible around +0.3 V_{RHE} and became even more evident after the ASTs. Also, both PtNi(Mo)-12 and PtNi(Mo)-14 displayed the characteristic Mo(IV)/Mo(VI) voltammetric wave inside the double-layer region (0.3–0.6 V_{RHE}), whereas PtNi(Mo)-7 missed that feature.[36] Again, after ASTs, these Mo peaks became more pronounced.[43] Linear sweep voltammetry (LSVs) in O_2-saturated electrolyte before and after the ASTs are presented in Figure S6. The LSVs display the characteristic regimes of kinetic, mixed, and mass transport control. The insets show the magnification of potentials around 0.9 V_{RHE}. In order to investigate morphology after the ASTs, the catalysts were collected from the working electrode and were subsequently deposited on a TEM grid (Figure S6 right column). Inspection revealed that the morphology of PtNi(Mo)-7 changed only slightly, with the LSVs before and after the AST showing only a minor decrease in catalytic reactivity at 0.9 V_{RHE}. By contrast, the principal emergence of concave-shaped octahedral NPs was observed for the PtNi(Mo)-12 and PtNi(Mo)-14 catalysts (Figures S6b and c, right column). The concavity of PtNi(Mo)-14 was more defined than that of PtNi(Mo)-12.

Table S2 presents the corresponding electrochemical data collected for the different catalysts obtained in this paper.

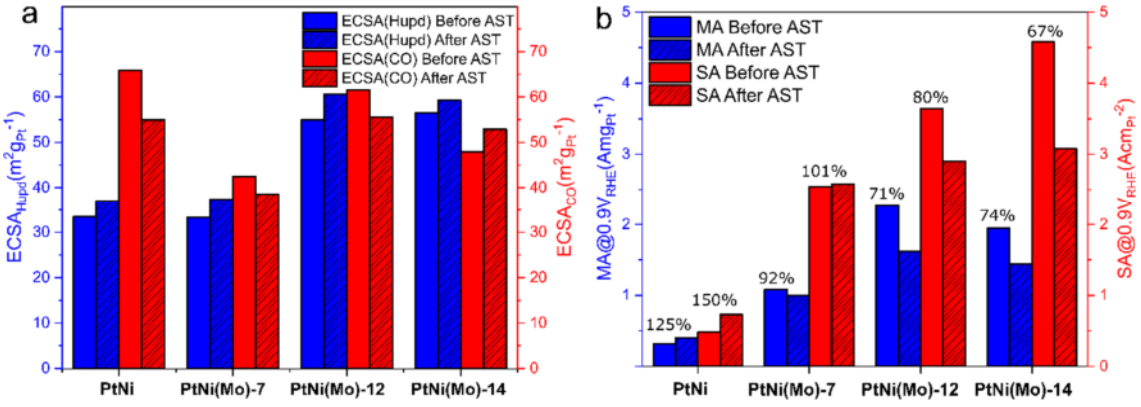

Figure 3. (a) $ECSA_{Hupd}$ (blue) and $ECSA_{CO}$ (red) before (solid) and after (dashed) ASTs (b) Mass (blue) and specific (red) activities before (solid) and after (dashed) ASTs (evaluated at 0.9 V_{RHE}).

Figure 3a presents the electrochemical surface areas (ECSAs), derived from CO and H_{upd} charges, while Figure 3b reports the corresponding specific (CO-based) and Pt mass-based electrocatalytic ORR activities. In general, the Ni-rich catalysts displayed the highest $ECSA_{CO}$. Out of the doped catalysts the Pt-rich (PtNi(Mo)-7) possess the lowest $ECSA_{Hupd.}$ Interestingly, a significant discrepancy between $ECSA_{CO}$ and $ECSA_{Hupd}$ was evident only for the smallest, bimetallic oh-PtNi-6 reference catalyst, with the $ECSA_{CO}$ almost twice the $ECSA_{Hupd}$. This is an indication of the presence of Ni atoms in surface or subsurface regions.[44] PtNi(Mo)-12 and the PtNi-6 octahedra showed the two highest $ECSA_{CO}$ of 61.7 and 65.9 $m^2g_{Pt}^{-1}$, respectively, comparable to the Pt/C reference catalyst (67.7 $m^2g_{Pt}^{-1}$). This is an exceptionally high value for an oh-shaped Pt alloy nanoparticle catalyst,[18, 28, 29] and is potentially of much significance for the design of sufficiently rough, high performing PEM fuel cell cathodes. More specifically, $ECSA_{CO}$ values of > 50 m^2gPt^{-1} at particle sizes of > 10 nm were claimed to be required to enable cathode layers with sufficient "Pt roughness factor" needed for high power performance.[45]

At the same time, all present oh-PtNi(Mo) catalysts exhibited higher electrocatalytic activities for the ORR than the Pt/C and the oh- Ni-rich PtNi-6 reference catalysts. For the Mo-doped catalysts, the ORR SA increases as particle size and Ni-content increases and reaches relatively high values (4.58 mA cmPt-2 for PtNi(Mo)-14, 20-times higher than Pt/C).

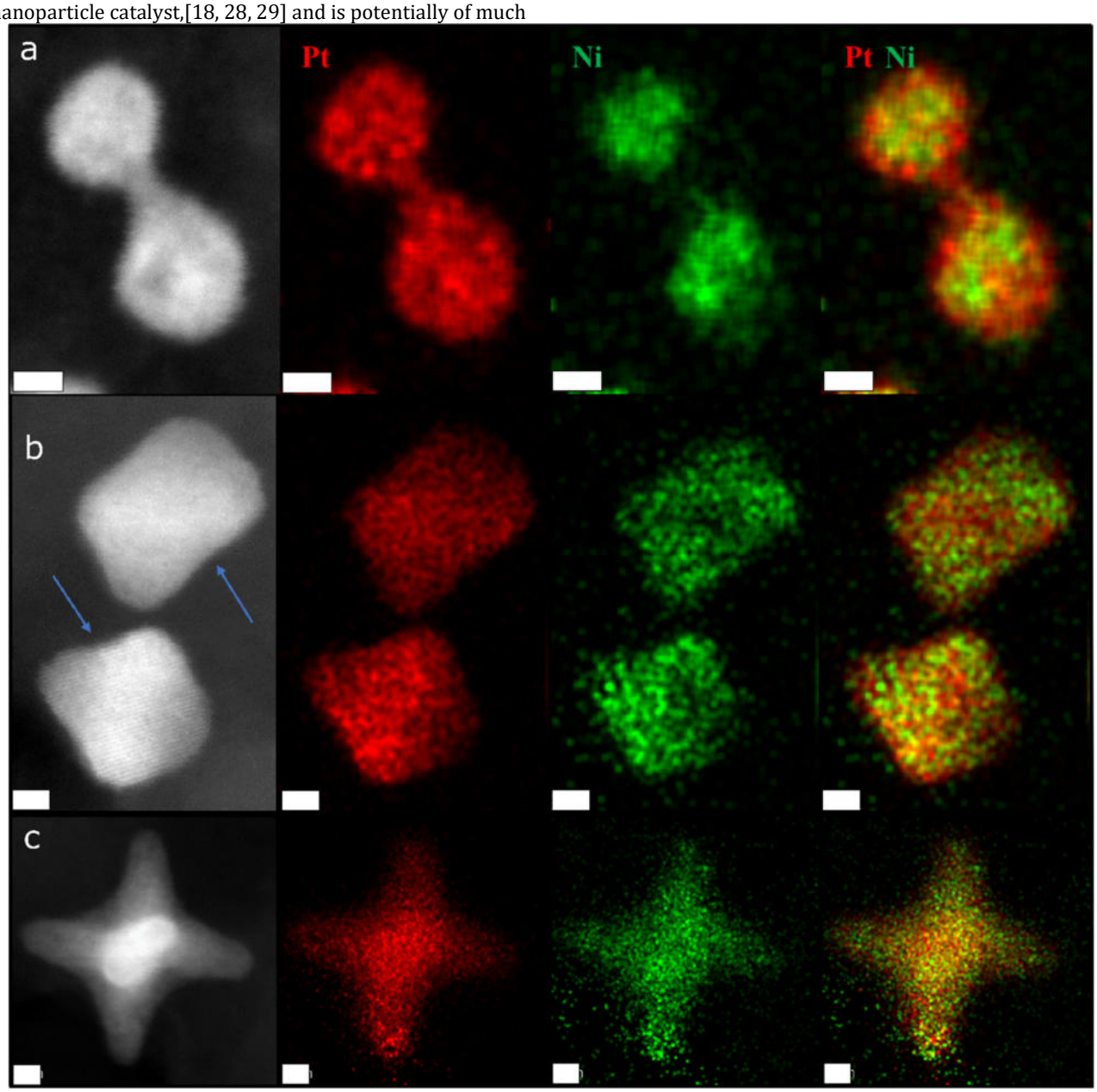

Figure 4. HAADF-STEM micrographs, STEM-EDX elemental mapping for Pt (red) and Ni (green), their overlay, after ASTs, CV in nitrogen-saturated atmosphere and LSV in oxidative atmosphere for (a) PtNi-6 (b) PtNi(Mo)-7 (c) PtNi(Mo)-14 (the scale bars correspond to 2 nm).

This relatively high value has been recently published for Pt-rich octahedra catalysts with similar size.[18, 46] The SA of PtNi(Mo)-14 after AST is greater than PtNi(Mo)-7 MA before AST. Moreover, the MA after ASTs for PtNi(Mo)-12 is greater than for PtNi(Mo)-7 MA after AST, suggesting the benefits of using Ni-rich catalysts. PtNi(Mo)-12 exhibit seven times greater MA compared to the PtNi-6 octahedra and Pt/C. When comparing the MAs of PtNi(Mo)-12 and PtNi(Mo)-14, a decrease is seen at bigger particles size as expected for bigger particles with almost the same composition and atomic distribution. The MA is the catalyst activity parameter that directly translates to catalyst cost since Pt is purchased by weight. Furthermore, MA is the product of the SA and the ECSA. The combination of a high ORR SA and high ECSA, which leads to high MA values, was also seen in the self-supported nano-porous Pt–CoO networks published recently.[47] The key to understanding the electrocatalytic properties of core-shell nanocatalysts lies in the atomic distribution of the surface and subsurface layers. Or more precisely, the Pt shell thickness and the distribution of the non-noble transition metals in the subsurface layers.[48] HAADF-STEM-EDX analysis of the thin-films retrieved from the working electrode after ASTs was used to monitor the changes occurring on the facets of the particles during ASTs, activity measurements under oxidative atmosphere and CV under N_2-saturated atmosphere. Table S2 shows a quantitative EDX analysis of the different catalysts after electrochemical tests.[49] These conditions have led to an evolution of the composition of all catalysts towards a stable Pt-rich composition. The PtNi-6 octahedra have lost their shape completely and transformed into spherical PtNi core-shell NPs (Figures 4a and S7). The surfaces after AST are more active due to the formation of a Pt shell, as shown in Figure 4a. PtNi(Mo)-7 has largely retained its octahedral shape and showed a Pt shell over a PtNi-alloyed core (Figure 4b), which is associated with the high stability expected from Pt-rich catalysts.[16] The arrows in Figure 4b show the points where pitting of the catalysts began. PtNi(Mo)-12 and PtNi(Mo)-14, transformed into a concave octahedra with a thin Pt layer shell over an alloyed PtNi hexapod core (Figures 4c, S8 and S9). In Figure S8, the line scan shows the different elemental ratio of Pt:Ni near the ⟨100⟩ zone axis.

The comparison of the shape loss of the Ni-rich catalysts PtNi-6 with PtNi(Mo)-12 and PtNi(Mo)-14 shows the advantages of Mo doping on the stability of the catalysts.[29-31, 36] The high residual activity for the concave octahedra is expected due to enhanced local composition and structural disorder.[50] The catalysts not only withstood the conditions of AST but also experienced oxidative atmospheres during ORR activity measurements that induced Ni dissolution.[16, 44] Furthermore, the strong interaction between CO_{ad} and surface Pt sites could alter the surface morphology and composition during CO-stripping measurements.[51]

On-line SFC-ICP- MS and IL -STEM. To get molecular insight in the relationships between the electrochemical test conditions and the resulting compositional transformations under AST conditions (inert atmosphere), the dissolution profiles of the different shaped catalysts were investigated using on-line ICP-MS measurements and correlated with the morphology degradation based on the identical location STEM (IL-STEM). IL-STEM allowed us to follow the morphology evolution of one and the same octahedron under the AST conditions. Figure 5a and 5b show HAADF micrographs of PtNi(Mo)-12 before and after AST, demonstrating the transformation of facets from flat to concave. EDX elemental mapping and quantitative analysis prior and after AST showed an atomic ratio (Pt:Ni) of 0.25:1 and 1.5:1, respectively, confirming Ni leaching during AST measurements (Figure 5c and 5d).

Figures S10–13 show the dissolution profiles for Pt, Ni, Mo recorded for PtNi-6, PtNi(Mo)-7, PtNi(Mo)-12 and PtNi(Mo)-14, respectively. In general, for all traced metals the most significant dissolution occurred when the SFC contacted the pristine drop-cast catalyst layer spots. The ensuing metal dissolution spike rapidly decreased until the end of the galvanostatic hold (j= 0 mA cm^{-2}). Thereafter, a small increase in metal dissolution was visible at the beginning of the AST cycles. Apart from this, no new dissolution events occurred over the course of the AST experiments. These observations in conjunction with IL -STEM measurements, suggest that the contact of the working electrode with the electrolyte is the main contributor to Ni dissolution and shape evolution for the PtNi(Mo)-12 catalyst. To follow the stability of the catalyst samples at more anodic applied potentials, an additional CV was recorded at the end of the AST protocol in the potential range of 0.6–1.5 V_{RHE} at a scan rate of 10 mV s^{-1}. The dissolution of all three metals started above 1 V_{RHE} (1.07 V_{RHE}, 1.00 V_{RHE} and 1.15 V_{RHE} for Pt, Ni and Mo, respectively), and the onset potential of dissolution does not change with the composition of the samples. Two distinct dissolution features can be observed for Pt, one in the anodic scan and one in the cathodic scan, which is consistent with previous literature results.[52, 53] In contrast, the dissolution of Ni and Mo could only be observed in the anodic scan in the form of single peaks. Surprisingly, Ni dissolution starts at very anodic potentials, past those of Pt. This indicates that all Ni present on the surface of the electrocatalyst was immediately passivated and oxidized, when the electrode came into contact with the electrolyte. Therefore, dissolution of Ni became only possible,

once a small amount of Pt at the surface dissolved, thereby making the underlying Ni sites accessible to the electrolyte solution. . To determine the amount of dissolved metals in each sample, all dissolution peaks were integrated (Figures 5e and S14). As expected, the dissolved molar amount of Ni was the largest, while those of Mo and Pt were significantly smaller.

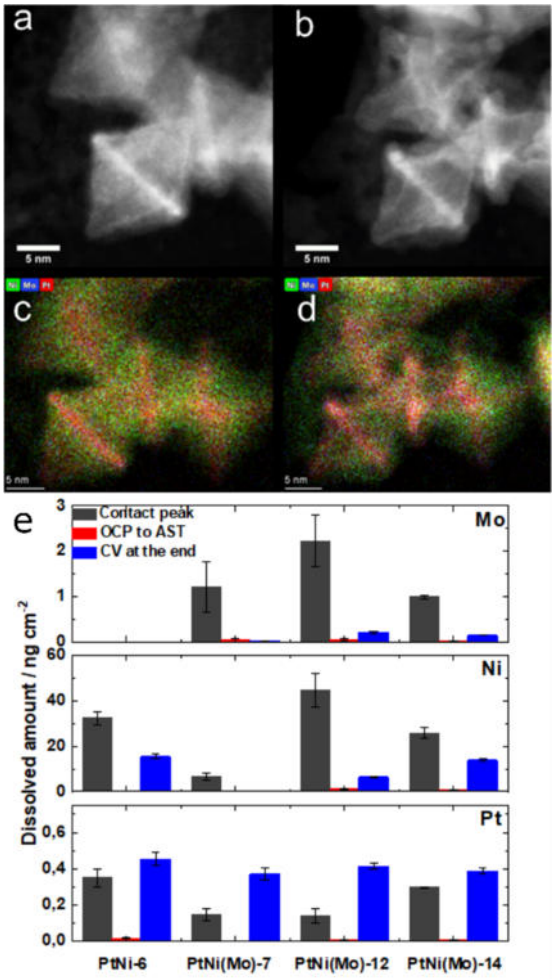

Figure 5. IL-HAADF micrograph of (a) before, (b) after AST and IL-STEM-EDX of (a) before, (b) after AST for PtNi(Mo)-12, (e) on-line ICP-MS dissolution measurements during ASTs for the different catalysts.

The amount of dissolved Pt was approximately two orders of magnitude smaller than the values calculated for Ni; the highest values were obtained for the PtNi-6 sample. The Ni dissolution scaled with the Pt:Ni ratio in the alloys and was less pronounced for the PtNi(Mo)-7 sample containing 25 at% Ni, showing a barely visible dissolution peak during the last CV in the wide potential window. Since the Mo content is low (below 2 at% for all samples), the Mo dissolution remained low in all cases. Finally, based on the dissolved amounts, post-AST compositions of all samples were calculated (Table S2). Similar conclusions can be made as in the case of the quantitative EDX analysis, i.e. the Pt:Ni ratio increased in all samples, while the compositions calculated from the ICP-MS data matched well with the ones derived from the EDX data for the PtNi(Mo)-7 sample, a notable difference can be observed for PtNi-6, PtNi(Mo)-12 and PtNi(Mo)-14 Ni-rich samples.

Based on the ICP-MS data, the increase in the Pt/Ni ratio is much smaller than that based on the EDX measurements ($Pt_{39.2}Ni_{59.6}Mo_{1.2}$ vs. $Pt_{76.9}Ni_{23.1}$ and $Pt_{32.8}Ni_{65.4}Mo_{1.8}$ vs. $Pt_{79.4}Ni_{20.6}$ for PtNi(Mo)-12 and PtNi(Mo)-14, respectively). This discrepancy was observed for the Ni-rich catalysts only, however, not for the Pt-rich catalyst (PtNi(Mo)-7), the initial composition of which was stable during AST conditions and during the different applied electrochemical measurements. The reason for the drastic compositional discrepancy is attributed to Ni-leaching during the electrochemical measurements performed additionally to the ASTs.

Conclusions

The present work highlights the need for new synthetic approaches to prepare large Ni-rich octahedral catalysts. Increasing the Ni precursor and the solvent volume independently led to an increase in the size of the octahedra, indicating a correlation between size and composition. The addition of Mo in a single-step colloidal synthesis of Ni-rich octahedral PtNi nano-catalysts promotes the shape stability during potential cycling. This was confirmed by post-mortem STEM-EDX analysis. The SA observed in addition to the size increase appears to originate from the relatively highly extended (111) facets. IL-STEM combined with on-line ICP-MS showed that only minor Ni dissolution was evident under the AST conditions. The Ni-rich Mo-doped nanocrystals do not retain their initial activities, but the residual activity is much higher compared to the initial activity of the un-doped Ni-rich PtNi octahedral catalyst. The ability to control size and composition in PtNi(Mo)-octahedral catalysts allowed us to observe the increase in ORR performance along with the increase in (111) facets and Ni content, and suggests the development of ≥ 30 nm PtNi(Mo)/C electrocatalysts to maximize ECSA and specific activity. Nevertheless, out of the scope of this paper, when Ni- rich catalyst is applied to an MEA, Ni leaching due to the electrochemical activation may cause contamination of the fuel cell membrane. Post-treatments, not only produce durable and compositionally stable catalysts, but boost the activity as well.

ASSOCIATED CONTENT

Supporting Information. The experimental details are provided, TEM images, STEM-EDS, XRD, CV curves, ORR polarization curves, CO-stripping of the catalysts and dissolution profiles. This material is available free of charge via the Internet at http://pubs.acs.org.

AUTHOR INFORMATION

Corresponding Author

pstrasser@tu-berlin.de
m.heggen@fz-juelich.de
polani@tu-berlin.de

Author Contributions

The manuscript was written through contributions of all authors. All authors have given approval to the final version of the manuscript.

Funding Sources

The authors are grateful for the financial support by the Deutsche Forschungsgemeinschaft (DFG) under the grant numbers HE 7192/1-2 and STR 596/5-2.

ACKNOWLEDGMENT

The authors thank Victor Shokhen for his support in producing graphical models for the different catalysts.

REFERENCES

1. Markovic, N., H. Gasteiger, and P.N. Ross, *Kinetics of Oxygen Reduction on Pt (hkl) Electrodes : Implications for the Kinetics of Oxygen Reduction on Pt (hkl) Electrodes : Implications for the Crystallite Size Effect with Supported Pt Electrocatalysts.* 1997(May): p. 1-8.
2. Stamenkovic, V.R., et al., *Trends in electrocatalysis on extended and nanoscale Pt-bimetallic alloy surfaces.* Nat Mater, 2007. **6**(3): p. 241-7.
3. Stamenkovic, V., et al., *Changing the activity of electrocatalysts for oxygen reduction by tuning the surface electronic structure.* Angew Chem Int Ed Engl, 2006. **45**(18): p. 2897-901.
4. Lindahl, N., et al., *High Specific and Mass Activity for the Oxygen Reduction Reaction for Thin Film Catalysts of Sputtered Pt3Y.* Advanced Materials Interfaces, 2017. **4**(13): p. 1700311.
5. Escudero-Escribano, M., et al., *Tuning the activity of Pt alloy electrocatalysts by means of the lanthanide contraction María.* Science, 2016. **352**(6281): p. 73-76.
6. Stamenkovic, V.R., et al., *Energy and fuels from electrochemical interfaces*. 2016. p. 57-69.
7. Cao, L., et al., *Differential Surface Elemental Distribution Leads to Significantly Enhanced Stability of PtNi-Based ORR Catalysts.* Matter, 2019. **1**(6): p. 1567-1580.
8. Mistry, H., et al., *Nanostructured electrocatalysts with tunable activity and selectivity*. 2016, Macmillan Publishers Limited. p. 1-15.
9. Debe, M.K., *Electrocatalyst approaches and challenges for automotive fuel cells*. 2012, Nature Publishing Group. p. 43-51.
10. Debe, M.K., et al., *High voltage stability of nanostructured thin film catalysts for PEM fuel cells.* Journal of Power Sources, 2006. **161**(2): p. 1002-1011.
11. Shao-Horn, Y., et al., *Instability of supported platinum nanoparticles in low-temperature fuel cells.* Topics in Catalysis, 2007. **46**(3-4): p. 285-305.
12. Han, B., et al., *Record activity and stability of dealloyed bimetallic catalysts for proton exchange membrane fuel cells.* Energy and Environmental Science, 2015. **8**(1): p. 258-266.
13. Stamenkovic, V.R., et al., *Improved Oxygen Reduction Activity on Pt3Ni(111) via Increased Surface Site Availability.* Science, 2007. **315**(5811): p. 493-497.
14. Markovic, H.A.G.a.N.M., *Just a Dream—or Future Reality?* Science, 2009. **324**(5923): p. 48-49.
15. Polani, S., et al., *Size dependent oxygen reduction and methanol oxidation reactions: catalytic activities of PtCu octahedral nanocrystals.* Catalysis Science & Technology, 2020. **10**(16): p. 5501-5512.
16. Cui, C., et al., *Compositional segregation in shaped Pt alloy nanoparticles and their structural behaviour during electrocatalysis.* Nat Mater, 2013. **12**(8): p. 765-771.
17. Huang, X., et al., *A rational design of carbon-supported dispersive Pt-based octahedra as efficient oxygen reduction reaction catalysts.* Energy and Environmental Science, 2014. **7**(9): p. 2957-2962.
18. Zhu, E., et al., *In situ development of highly concave and composition-confined PtNi octahedra with high oxygen reduction reaction activity and durability.* Nano Research, 2016. **9**(1): p. 149-157.
19. Wang, J., et al., *From rotating disk electrode to single cell: Exploration of PtNi/C octahedral nanocrystal as practical proton exchange membrane fuel cell cathode catalyst.* Journal of Power Sources, 2018. **406**(October): p. 118-127.
20. Jia, Y., et al., *Composition-tunable synthesis of Pt–Cu octahedral alloy nanocrystals from PtCu to PtCu 3 via underpotential-deposition-like process and their electro-catalytic properties.* RSC Adv., 2015. **5**(23): p. 18153-18158.
21. Zhang, J., et al., *Synthesis and oxygen reduction activity of shape-controlled Pt 3Ni nanopolyhedra.* Nano Letters, 2010. **10**(2): p. 638-644.
22. Wu, J., A. Gross, and H. Yang, *Shape and composition-controlled platinum alloy*

nanocrystals using carbon monoxide as reducing agent. Nano Letters, 2011. **11**(2): p. 798-802.
23. Choi, S.I., et al., *Synthesis and characterization of 9 nm Pt-Ni octahedra with a record high activity of 3.3 A/mgPt for the oxygen reduction reaction.* Nano Letters, 2013. **13**(7): p. 3420-3425.
24. Shao, M., et al., *Electrochemical surface area measurements of platinum- and palladium-based nanoparticles.* Electrochemistry Communications, 2013. **31**: p. 46-48.
25. Chou, S.W., et al., *Uniform size and composition tuning of PtNi octahedra for systematic studies of oxygen reduction reactions.* Journal of Catalysis, 2014. **309**: p. 343-350.
26. Wu, Y., et al., *Syntheses of water-soluble octahedral, truncated octahedral, and cubic Pt-Ni nanocrystals and their structure-activity study in model hydrogenation reactions.* Journal of the American Chemical Society, 2012. **134**(21): p. 8975-8981.
27. Kavian, R., et al., *Pt-Ni octahedral nanocrystals as a class of highly active electrocatalysts toward the hydrogen evolution reaction in an alkaline electrolyte.* Journal of Materials Chemistry A, 2016. **4**(32): p. 12392-12397.
28. Lim, J., et al., *Ga-Doped Pt-Ni Octahedral Nanoparticles as a Highly Active and Durable Electrocatalyst for Oxygen Reduction Reaction.* Nano Lett, 2018. **18**(4): p. 2450-2458.
29. Huang, X., et al., *High-performance transition metal – doped Pt 3 Ni octahedra for oxygen reduction reactionHuang, X., Cao, L., Chen, Y., Zhu, E., Lin, Z., Li, M., … Mueller, T. (2015). High-performance transition metal – doped Pt 3 Ni octahedra for oxygen reduction reactio.* Science, 2015. **348**(6240): p. 1230-1234.
30. Cao, L. and T. Mueller, *Theoretical Insights into the Effects of Oxidation and Mo-Doping on the Structure and Stability of Pt-Ni Nanoparticles.* Nano Lett, 2016. **16**(12): p. 7748-7754.
31. Jia, Q., et al., *Roles of Mo Surface Dopants in Enhancing the ORR Performance of Octahedral PtNi Nanoparticles.* Nano Lett, 2018. **18**(2): p. 798-804.
32. Dionigi, F., et al., *Controlling Near-Surface Ni Composition in Octahedral PtNi(Mo) Nanoparticles by Mo Doping for a Highly Active Oxygen Reduction Reaction Catalyst.* Nano Letters, 2019. **19**(10): p. 6876-6885.
33. Beermann, V., et al., *Rh-Doped Pt-Ni Octahedral Nanoparticles: Understanding the Correlation between Elemental Distribution, Oxygen Reduction Reaction, and Shape Stability.* Nano Lett, 2016. **16**(3): p. 1719-25.
34. Shviro, M., S. Polani, and D. Zitoun, *Hollow octahedral and cuboctahedral nanocrystals of ternary Pt-Ni-Au alloys.* Nanoscale, 2015. **7**(32): p. 13521-13529.
35. Shviro, M., et al., *Morphological, Structural, and Compositional Evolution of Pt–Ni Octahedral Electrocatalysts with Pt-Rich Edges and Ni-Rich Core: Toward the Rational Design of Electrocatalysts for the Oxygen Reduction Reaction.* Particle and Particle Systems Characterization, 2019. **36**(3): p. 1-6.
36. Dionigi, F., et al., *Controlling Near-Surface Ni Composition in Octahedral PtNi(Mo) Nanoparticles by Mo Doping for a Highly Active Oxygen Reduction Reaction Catalyst.* Nano Lett, 2019. **19**(10): p. 6876-6885.
37. Wang, D. and Y. Li, *One-pot protocol for au-based hybrid magnetic nanostructures via a noble-metal-induced reduction process.* Journal of the American Chemical Society, 2010. **132**(18): p. 6280-6281.
38. Oh, A., et al., *Skeletal octahedral nanoframe with cartesian coordinates via geometrically precise nanoscale phase segregation in a Pt@Ni core-shell nanocrystal.* ACS Nano, 2015. **9**(3): p. 2856-2867.
39. Lamer, V.K. and R.H. Dinegar, *Theory, Production and Mechanism of Formation of Monodispersed Hydrosols.* Journal of the American Chemical Society, 1950. **72**(11): p. 4847-4854.
40. MacArthur, K.E., M. Heggen, and R.E. Dunin-Borkowski, *Differentiating the structure of PtNi octahedral nanoparticles through combined ADF–EDX simulations.* Advanced Structural and Chemical Imaging, 2018. **4**(1).
41. Yankovich, A.B., et al., *Non-rigid registration and non-local principle component analysis to improve electron microscopy spectrum images.* Nanotechnology, 2016. **27**(36): p. 1-14.
42. Hoglund, F.d.l.P., et al., *Electron Microscopy (Big and Small) Data Analysis With the Open Source Software Package HyperSpy*. 2020.
43. Yang, W., et al., *The behavior of chromium and molybdenum in the propagation process of localized corrosion of steels.* Corrosion Science, 1984. **24**(8): p. 691-707.
44. Rudi, S., et al., *Comparative Study of the Electrocatalytically Active Surface Areas (ECSAs) of Pt Alloy Nanoparticles Evaluated by Hupd and CO-stripping voltammetry.* Electrocatalysis, 2014. **5**(4): p. 408-418.
45. Kongkanand, A. and M.F. Mathias, *The Priority and Challenge of High-Power Performance of Low-Platinum Proton-Exchange Membrane Fuel Cells.* J Phys Chem Lett, 2016. **7**(7): p. 1127-37.
46. Zhao, X., et al., *Simultaneous Improvements in Performance and Durability of an Octahedral PtNix/C Electrocatalyst for Next-Generation Fuel Cells by Continuous, Compressive, and Concave Pt Skin Layers.* ACS Catalysis, 2017. **7**(7): p. 4642-4654.
47. Sievers, G.W., et al., *Self-supported Pt-CoO networks combining high specific activity with high surface area for oxygen reduction.* Nat Mater, 2020.
48. Gan, L., et al., *Core-shell compositional fine structures of dealloyed Pt xNi 1-x nanoparticles*

and their impact on oxygen reduction catalysis. Nano Letters, 2012. **12**(10): p. 5423-5430.
49. MacArthur, K.E., et al., *Quantitative Energy-Dispersive X-Ray Analysis of Catalyst Nanoparticles Using a Partial Cross Section Approach.* Microscopy and Microanalysis, 2016. **22**(1): p. 71-81.
50. Kühl, S., et al., *Concave curvature facets benefit oxygen electroreduction catalysis on octahedral shaped PtNi nanocatalysts.* Journal of Materials Chemistry A, 2019. **7**(3): p. 1149-1159.
51. Mayrhofer, K.J.J., et al., *Adsorbate-induced surface segregation for core-shell nanocatalysts.* Angewandte Chemie (International ed. in English), 2009. **48**(19): p. 3529-31.
52. Schalenbach, M., et al., *The Electrochemical Dissolution of Noble Metals in Alkaline Media.* Electrocatalysis, 2018. **9**(2): p. 153-161.
53. George, M., et al., *Effect of Ionic Liquid Modification on the ORR Performance and Degradation Mechanism of Trimetallic PtNiMo/C Catalysts.* ACS Catal, 2019. **9**(9): p. 8682-8692.

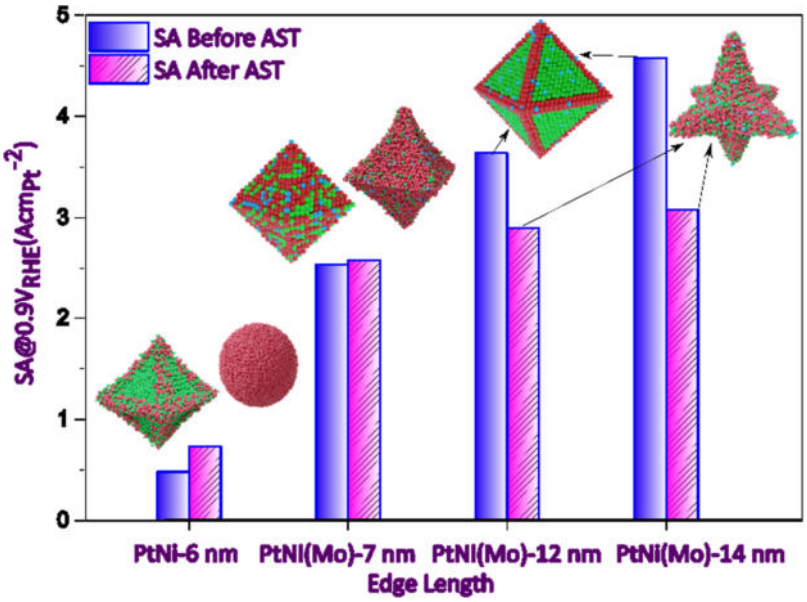

Table of Contents artwork